Advances in Science and Technology Research Journal

Advances in Science and Technology Research Journal, 2027, 21(1), 606–622
https://doi.org/10.12913/22998624/231642
ISSN 2299-8624, License CC-BY 4.0

Received: 2026.08.06
Accepted: 2026.11.16
Published: 2026.12.01

Pore morphology, spatial distribution and size characteristics as a function of build orientation and heat treatment in laser beam powder bed fusion-manufactured 316L stainless steel

Robert Saraczyn[1*], Martyna Deroszewska[1], Krzysztof Kulikowski[2], Tomasz Borowski[2], Ahmad Edelbi[1], Dawid Myszka[1]

[1] Faculty of Mechanical and Industrial Engineering, Warsaw University of Technology, Pl. Politechniki 1, 00-665 Warsaw, Poland
[2] Faculty of Materials Science and Engineering, Warsaw University of Technology, Pl. Politechniki 1, 00-665 Warsaw, Poland
* Corresponding author's e-mail: robert.saraczyn.dokt@pw.edu.pl

ABSTRACT:

This study examines pore morphology, size characteristics, and spatial arrangement in laser beam powder bed fusion (LB-PBF) 316L stainless steel cylindrical preforms subsequently machined into tensile samples. The preforms were fabricated in vertical, horizontal, and 45° build orientations and analysed in the as-printed condition and after annealing, followed by water quenching. Quantitative pore characterisation was performed using SEM-based ImageJ analysis, with descriptors including pore size, shape, and spatial distribution. These data were examined alongside tensile properties and melt-pool-scale microstructural observations. The results show orientation-dependent differences between the as-printed and heat-treated post-mortem pore populations. The most pronounced changes were observed for the 45° and vertical conditions, where pore count increased from 7.25 to 150.38 and from 10.60 to 325.21 pores per analysed field, respectively, while mean pore area decreased from 0.532 to 0.075 μm² and from 0.769 to 0.108 μm². In all orientations, annealing reduced 0.2% proof strength and ultimate tensile strength while increasing elongation; elongation increased from 37.8% to 49.7% for the 45° condition, from 31.8% to 39.6% for the horizontal condition, and from 42.4% to 55.3% for the vertical condition. The strength reduction is consistent with heat-treatment-induced modification of the LB-PBF microstructural state, while mechanisms such as recovery and residual-stress relief may have contributed to the observed response. The heat-treated conditions also exhibited smaller and more regular detected pore features, which may have contributed to the increased ductility. The study demonstrates that morphology-resolved pore analysis provides a more informative basis for interpreting defect-sensitive mechanical behaviour in LB-PBF 316L than conventional porosity metrics alone.

Keywords: laser beam powder bed fusion, heat treatment, build orientation, porosity, image analysis.

INTRODUCTION

Additive manufacturing (AM) of metals has gained widespread attention due to its capability to fabricate complex geometries, reduce material waste, and enable design freedoms unattainable by conventional manufacturing routes [1]. Among metal AM technologies, Laser Beam Powder Bed Fusion (LB-PBF) is one of the most widely adopted processes, producing near-net-shape components with high dimensional accuracy and fine microstructural features [2]. In LB-PBF, metallic powder is selectively melted layer by layer using a high-energy laser beam, resulting in extremely high thermal gradients and rapid cooling rates, typically on the order of 10^5–10^6 K·s^{-1} [3–6]. The rapid heating and cooling cycles in LB-PBF strongly influence melt-pool behaviour, solidification kinetics, and defect formation, leading to microstructures and defect

populations that differ markedly from those produced by conventional processing routes [7–9]. While these conditions enable refined microstructures, they also promote the formation and retention of defects, particularly porosity. Porosity is one of the most frequently reported defects in LB-PBF-fabricated metals, and its formation is closely tied to the complex thermal and physical phenomena that occur during layer-wise melting and solidification [10]. Several pore types are commonly observed, including gas-induced pores, keyhole-induced pores, and lack-of-fusion (LoF) defects, each associated with distinct processing conditions and melt-pool instabilities. Gas pores are typically spherical and originate from entrapped gas within powder particles or the melt-pool [11], whereas keyhole pores form due to unstable vapour cavities under excessive energy input [12]. LoF defects result from insufficient melting between adjacent tracks or layers and are often irregular in shape [13]. In the present work, pore classification is based on morphology rather than inferred formation mechanisms. The formation of each pore type is strongly influenced by process parameters such as laser power, scan speed, hatch spacing, and layer thickness [14]. Low-energy-density conditions tend to promote lack-of-fusion (LoF) defects due to incomplete melting, whereas excessively high energy density can drive the process into keyhole-mode melting, increasing the likelihood of keyhole porosity [15]. Gas-induced porosity in additive manufacturing is strongly correlated with the internal porosity of powder particles originating from the atomisation process. These defects are primarily distinguished from processing-induced porosity by their spherical morphology [16]. Beyond parameter selection, build orientation plays a critical role by altering heat flow, melt-pool geometry, and interlayer thermal interaction [17]. Components built vertically, horizontally, and at inclined orientations experience distinct thermal histories, which can lead to orientation-dependent variations in pore morphology, size, and segregation. These effects become particularly relevant when interpreting defect populations in LB-PBF-fabricated 316L stainless steel, a material widely used due to its excellent corrosion resistance and processability. Post-processing heat treatment provides an additional pathway for modifying defect populations by promoting localised plastic relaxation, which can alter pore morphology and reduce defect severity [18–19]. Depending on temperature, holding time, and cooling conditions, post-process heat treatment may modify the apparent pore population through changes in pore morphology, pore growth, coalescence, or redistribution [20–24]. While the influence of heat treatment on microstructure has been extensively studied, its specific effects on pore morphology in LB-PBF 316L stainless steel, particularly as a function of build orientation, remain incompletely understood [25]. Despite extensive literature on LB-PBF process optimisation and porosity formation, systematic studies addressing the combined influence of build orientation and post-processing heat treatment on pore morphology and defect evolution in 316L stainless steel are limited [26–29]. Most previous work has focused on processing parameters, microstructure, mechanical performance, or general porosity levels, while the specific role of pore morphology in governing material properties remains insufficiently addressed. In particular, the combined influence of build orientation and heat treatment on pore shape evolution, spatial distribution, and morphology-sensitive descriptors has not been comprehensively quantified.

The contribution of the work is a comparative, morphology-resolved assessment of post-mortem defect populations in LB-PBF 316L stainless steel across three build orientations and two material conditions. Beyond conventional pore area fraction, the analysis considers pore count, projected size, circularity, solidity and Feret dimensions, enabling orientation-dependent defect geometry to be examined alongside tensile behaviour and melt-pool-scale microstructural observations. By relating these morphology descriptors to build orientation and heat-treatment condition, the study provides insight into the role of defect morphology in process optimisation, property prediction and component reliability.

METHODOLOGY

This work examines the influence of build orientation and subsequent heat treatment on the morphology, spatial distribution, and size characteristics of pores in an Fe-based alloy. Austenitic stainless steel 316L was selected as a model material because it retains a fully austenitic crystal structure over a wide temperature range, thereby eliminating microstructural phase transformations as an additional variable in the analysis.

Furthermore, when processed under optimised parameters, 316L typically exhibits relatively stable melt-pool behaviour, promoting more consistent porosity characteristics.

Materials and technologies

The material used in this study was 316L austenitic stainless steel powder with a particle size distribution of 15–45 µm. The chemical and physical properties of the powder are listed in Table 1 and Table 2. Cylindrical preforms with a length of 100 mm and a diameter of 12 mm were fabricated by laser beam powder bed fusion using an Aconity MIDI system. The printing parameters included a laser power of 150 W, a scanning speed of 800 mm·s^{-1}, and a layer thickness of 30 µm. A hatch distance of 80 µm was applied using a 5 mm stripe scanning strategy with a 67° rotation between successive layers. The processing parameters are listed in Table 3

To investigate the impact of build direction, cylindrical preforms were printed in three orientations: vertical (90°), horizontal (0°), and 45°. The vertical (90°), horizontal (0°), and 45° configurations relative to the build plate are shown in Figure 1. A total of 12 cylindrical preforms were fabricated, comprising four preforms for each build orientation: vertical, horizontal, and 45°.

Following the LB-PBF process, two of the four cylindrical preforms fabricated in each build orientation were subjected to solution annealing using a Nabertherm GmbH N 11/HR furnace, while the remaining two were retained in the as-printed condition. The heat-treatment cycle consisted of placing the preforms in a furnace preheated to 1120 °C, followed by a nominal holding time of 30 min at the target temperature and

Table 1. Chemical composition of 316L powder used

%Fe	%Cr	%Ni	%Mo	%Mn	%Si	%Cu	%O	%N	%C	%P	%S
Bal.	17.5–18	12.5–13	2.25–2.5	2.0	<0.75	<0.50	<0.10	<0.10	<0.03	<0.025	<0.010

Table 2. Nominal physical properties of 316L stainless steel powder used

Particle size	Density	Thermal conductivity	Melting range	Thermal expansion
15–45 µm	7.98 g·cm^{-3}	21 W·m^{-1}·K^{-1}	1380–1410 °C	16 × 10^{-6} K^{-1}

Table 3. LB-PBF processing parameters used for fabrication of 316L stainless steel cylindrical preforms

Laser power	Scanning speed	Layer thickness	Hatch distance	Scanning strategy
150 W	800 mm·s^{-1}	30 µm	80 µm	5 mm stripes

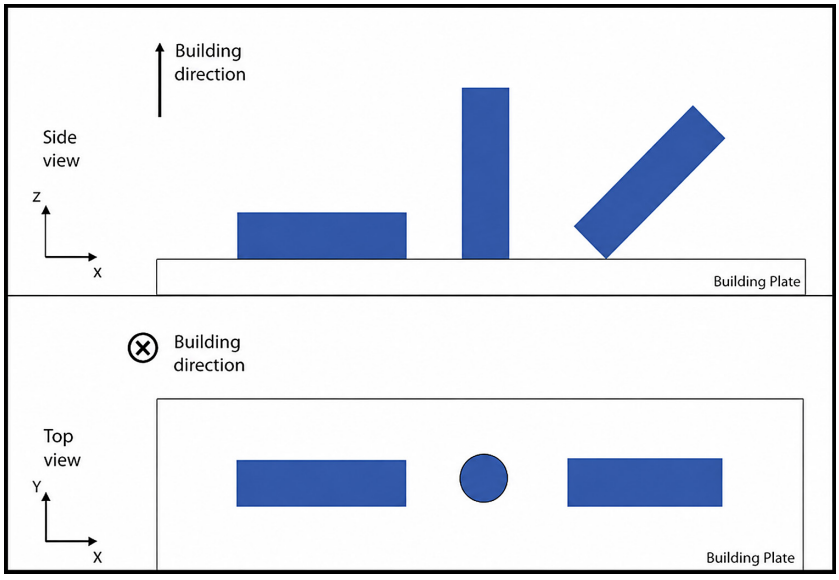


Figure 1. Schematic illustration of preform build orientations relative to the build plate and loading direction

subsequent water quenching to room temperature. Since the temperature was controlled by the furnace rather than directly measured inside the preforms, the thermal profile should be regarded as a nominal treatment cycle. The temperature–time profile of the HT process is presented in Figure 2. The treatment was selected as a high-temperature solution-annealing condition intended to modify the solidification-induced LB-PBF microstructure. Comparable parameters have previously been applied to additively manufactured 316L [24], while rapid cooling is conventionally employed following solution annealing of austenitic stainless steels.

Research instrumentation

The cylindrical preforms were machined by turning to obtain tensile-test samples with the geometry shown in Figure 3, in line with ISO 6892-1:2019. This machining step was used to remove the oxidised surface layer and near-surface defects associated with the LB-PBF process, thereby reducing the influence of surface condition on the subsequent mechanical and microstructural analyses.

Separate 5 mm-thick sections were cut from one side of the grip regions of the tensile samples specifically for optical microscopy analysis. Metallographic specimens were prepared from these sections with the observation plane oriented to reveal the melt-pool morphology; consequently, the microstructures were analysed in relation to the build direction. This preparation route was independent of that used for the metallographic specimens subsequently obtained from the tensile-test fracture regions for SEM-based porosity characterisation. Optical microscopy was performed using an Olympus IX70 microscope operated in bright-field mode to examine the overall microstructural morphology and melt-pool boundaries.

Tensile tests were performed using an Instron 1115 testing machine on both as-printed (AP)

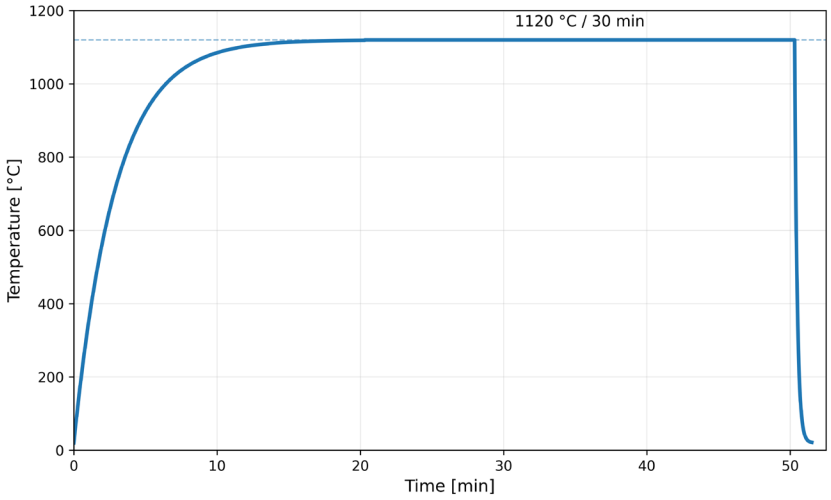


Figure 2. Nominal temperature–time profile of the heat-treatment cycle. The curve represents the estimated preform heating response in a furnace preheated to 1120 °C

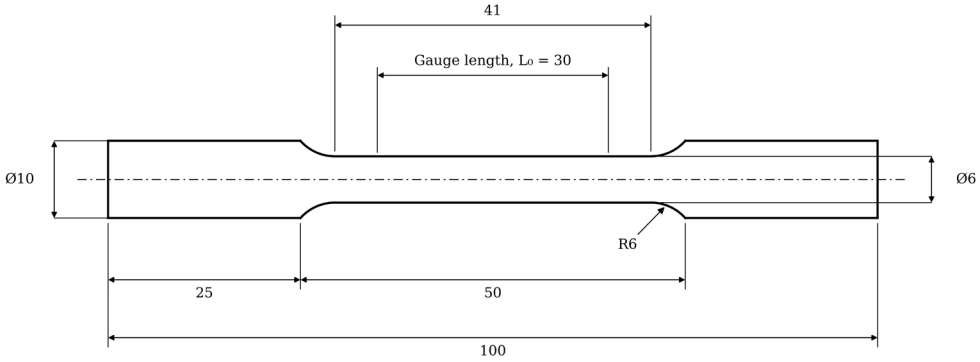


Figure 3. Tensile sample dimensions

and heat-treated (HT) samples. The ultimate tensile strength (R_m), 0.2% proof strength ($R_{0.2}$), and elongation at fracture were determined. All tests were conducted at a constant crosshead speed of 5 $mm \cdot min^{-1}$. As no extensometer was used, elongation and the 0.2% proof strength were determined from crosshead-displacement-based strain, which includes contributions from the compliance of the testing system and grips. Accordingly, these values should be regarded as approximate comparative measurements rather than high-precision extensometric data. Two tensile samples were tested for each condition. Owing to the limited number of tensile samples, the mechanical results are interpreted as comparative trends rather than as a statistically comprehensive assessment of material variability.

Post-mortem porosity analysis was performed on metallographic specimens prepared from tensile-tested samples. This approach was selected to evaluate pore populations in regions representative of the mechanically loaded material after failure and to compare defect morphology, size distribution, and spatial arrangement as a function of build orientation and heat-treatment condition. The analysis was therefore focused on relative differences between specimen variants rather than full three-dimensional pore reconstruction. Since porosity characterisation was performed on post-mortem sections prepared from tensile-tested samples, the detected pore population may include both process-induced pores and deformation-assisted voids formed during tensile loading. Therefore, the analysis is interpreted as a comparative assessment of post-mortem defect populations rather than direct three-dimensional tracking of thermally induced pore evolution. The same sampling and imaging strategy was applied to all material variants to enable relative comparison between build orientations and heat-treatment conditions.

For each material condition — vertical as-printed (VAP), vertical heat-treated (VHT), horizontal as-printed (HAP), horizontal heat-treated (HHT), 45° as-printed (45AP), and 45° heat-treated (45HT) — four metallographic specimens were prepared from two tensile-tested samples, with two specimens obtained from each sample. The specimens were mounted in epoxy resin, ground, polished, and prepared for metallographic observation. Four regions were imaged on each prepared specimen, resulting in 16 SEM images per material condition. This sampling strategy was adopted to reduce the influence of local microstructural heterogeneity and minimise random bias in the quantitative pore analysis.

SEM observations were conducted using an Axia ChemiSEM system (Thermo Fisher Scientific) at 1,000× magnification. The microscope was operated at an accelerating voltage of 10 kV using consistent working-distance and beam-current settings. Observations were performed on equivalent metallographic planes to support a consistent comparison of pore morphology, size, and spatial distribution.

Circular backscattered electron (CBS) imaging was used for quantitative pore characterisation because it provided more reliable pore–matrix contrast for ImageJ-based segmentation than conventional backscattered electron (BSE) imaging under the applied preparation and imaging conditions. Preliminary BSE observations showed ambiguity between true pores and surface-related preparation artefacts, including polishing marks, pull-outs, and local relief, which could result in misclassification during thresholding. CBS imaging reduced this ambiguity by improving pore-boundary definition and was therefore selected for the subsequent quantitative analysis.

Pore characteristics, including pore count, mean pore area, and morphology descriptors, were quantified using ImageJ software. SEM images acquired at 1,000× magnification were imported into ImageJ and numerically adjusted for brightness and contrast to improve pore–matrix differentiation. Prior to particle analysis, all images were calibrated using the SEM scale bar. The same field area was analysed in all images. The same automatic thresholding procedure based on a modified IsoData iterative algorithm was applied to all images. The algorithm separates foreground features from the background by iteratively calculating the mean grey-level intensities of the two pixel classes and updating the threshold until convergence. The same image-processing conditions were applied to all images to ensure comparability among the material conditions. The images were then binarised to separate the metallic matrix from pore regions, generating black-and-white masks for quantitative analysis, as illustrated in Figure 4. In the binarised images, the detected pore regions were represented as white features against a black matrix background. These features were subsequently evaluated using the particle analysis function to determine the relevant morphological parameters.

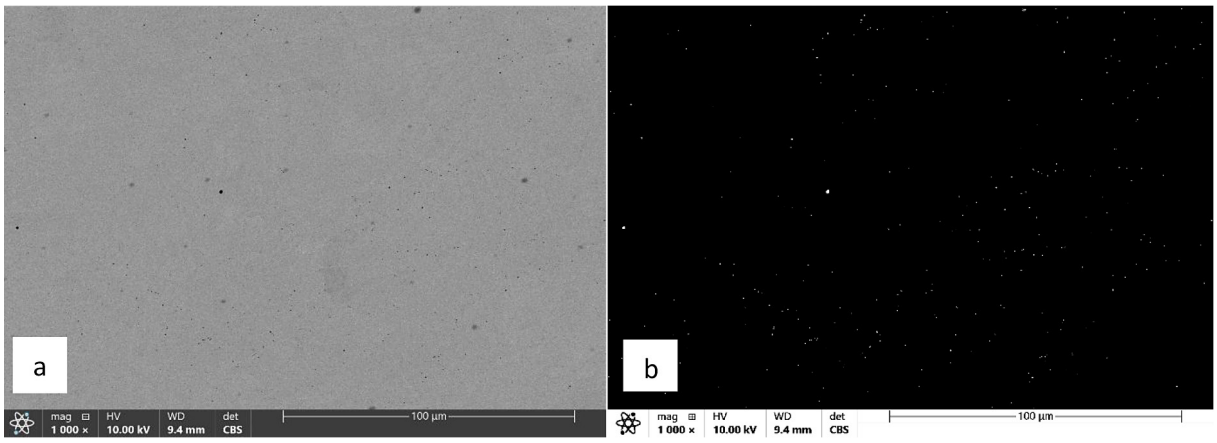


Figure 4. Representative workflow for ImageJ-based porosity analysis: (a) SEM image acquired at 1,000× magnification using CBS imaging and (b) corresponding binarised image after pore–matrix segmentation

For each SEM field, cumulative pore area was calculated as the sum of the projected areas of all detected pore features, whereas mean pore area represented the arithmetic mean projected area of the individual features detected within that field. The values reported in Table 4 are arithmetic means of the corresponding field-level ImageJ outputs for each material condition. Field-to-field heterogeneity was described using the coefficient of variation of pore area fraction, calculated as the sample standard deviation divided by the arithmetic mean across the analysed SEM fields for each material condition.

RESULTS AND DISCUSSION

SEM observations revealed that, across all analysed variants, the dominant defects were rounded pores with smooth and continuous boundaries, as also reflected by the high circularity and solidity values. This is morphologically consistent with gas-type porosity reported in LB-PBF–processed materials.

A clear dependence of pore morphology, size, and spatial distribution on build orientation was observed. Differences between the as-printed and heat-treated conditions were also evident, with a broadly similar trend across all build orientations. The heat-treated conditions generally exhibited a more dispersed population of smaller detected pore features throughout the analysed regions. Although the overall AP–HT trend appeared comparable for all orientations, distinct orientation-dependent differences were identified. These differences are discussed in detail in the following subsections.

45° build orientation

SEM observations of the specimens built at 45° to the build plate indicate a marked change in the pore population after heat treatment, as shown in Figure 5(a,b) and quantified in Table 4. In the as-printed condition, the mean number of detected pores was relatively low, with 7.25 pores per analysed field, whereas after heat treatment this value

Table 4. Mean ImageJ-derived pore characteristics for each condition based on metallographic specimens

Condition	Mean pore count	Mean total pore area [µm²]	Mean pore area [µm²]	Area fraction [%]	Perimeter [µm]	Circularity [−]	Solidity [−]	Feret diameter [µm]	Feret angle [°]	Min. Feret diameter [µm]
45° AP	7.25	4.83	0.532	0.017	2.016	0.941	0.921	0.754	123.25	0.541
45° HT	150.38	9.98	0.075	0.035	0.699	0.994	0.964	0.327	128.15	0.206
Horizontal AP	11.13	8.05	1.153	0.028	2.457	0.880	0.883	0.958	108.61	0.619
Horizontal HT	19.88	7.34	0.381	0.026	1.208	0.955	0.941	0.476	124.21	0.333
Vertical AP	10.60	7.60	0.769	0.026	2.199	0.891	0.884	0.855	117.26	0.541
Vertical HT	325.21	36.62	0.108	0.128	0.797	0.980	0.952	0.364	129.23	0.226

increased substantially to 150.38 pores per field. At the same time, the mean pore area decreased from 0.532 μm² to 0.075 μm², indicating a shift from a limited number of larger pores towards a more numerous population of finer defects.

This change is also reflected in the pore morphology descriptors. The mean perimeter, Feret diameter, and minimum Feret diameter also decreased after heat treatment, consistently indicating a reduction in the characteristic size of the detected pores. However, the total detected pore area increased from 4.83 μm² to 9.98 μm², and the area fraction increased from 0.017% to 0.035%. Therefore, the heat-treated condition should not be interpreted as having lower overall porosity, but rather as exhibiting a modified pore population characterised by a higher number of smaller pores.

The shape descriptors show that the pores became more geometrically regular after heat treatment. Circularity increased from 0.941 to 0.994, while solidity increased from 0.921 to 0.964. These values indicate that the detected pores in the heat-treated 45° specimens were, on average, closer to circular and more compact in projection. This observation is consistent with the SEM image in Figure 5(b), where large, isolated pores are less evident than in the as-printed condition. Since pore irregularity and elongation can locally intensify stress concentration, the transition towards smaller and more rounded pores may contribute to the improved ductility observed after heat treatment. However, this interpretation should be treated as contributory rather than exclusive, because heat treatment also modifies the printed microstructural state.

The mechanical data show a reduction in strength after heat treatment, with Rm decreasing from 683.5 MPa to 618.0 MPa and $R_{0.2}$ decreasing from 620.5 MPa to 387.5 MPa. In contrast, maximum elongation increased from 37.8% to 49.7%, corresponding to an increase of approximately 32% relative to the as-printed condition. The possible mechanisms underlying this strength–ductility response are discussed comparatively. The increase in elongation is compatible with both the reduced strength level and the observed differences in pore morphology; however, the present data do not allow these contributions to be fully separated.

In the as-printed condition, the microstructure exhibited a characteristic fish-scale morphology with clearly visible melt-pool boundaries, as shown in Figure 9(a). Pores were not uniformly distributed, and local variations in the detected pore population were observed in relation to the melt-pool architecture. Rounded pores were frequently located near melt-pool bottoms, whereas more irregular defects were associated with interlayer regions. This indicates that the spatial distribution of porosity in the 45° specimens was influenced by the melt-pool geometry and layer-wise build sequence.

After heat treatment, the melt-pool contrast was substantially reduced, as shown in Figure 9(b), resulting in a more homogenised microstructural appearance relative to the as-printed state. The pore population also appeared more spatially dispersed, with fewer clearly localised clusters in the analysed sections. This suggests that heat treatment altered both the visibility of the melt-pool structure and the apparent distribution of pore features. Nevertheless, the interpretation of pore redistribution should remain cautious, as the analysis is based on two-dimensional metallographic specimens and does not provide full three-dimensional tracking of individual pores before and after heat treatment.

Overall, the 45° condition showed a pronounced AP–HT difference in the detected post-mortem pore population, with the HT condition characterised by a higher number of smaller, more circular and compact features, together with reduced strength and increased elongation.

Horizontal build orientation

SEM observations of the horizontal metallographic specimens indicate that the detected post-mortem pore population showed a different AP–HT trend from that observed for the 45° build orientation, as shown in Figure 5(c,d) and quantified in Table 4. In the as-printed condition, the mean number of detected pores was 11.13 pores per analysed field, increasing moderately to 19.88 pores per field after heat treatment. This increase was considerably less pronounced than in the 45° specimens, indicating a smaller difference in the detected post-mortem pore population between the AP and HT horizontal conditions.

The mean pore area decreased from 1.153 μm² in the as-printed condition to 0.381 μm² after heat treatment, indicating a reduction in the average projected pore size. This trend was also reflected by decreases in mean perimeter, Feret diameter, and minimum Feret diameter, indicating a reduction in the characteristic size of the detected pores.

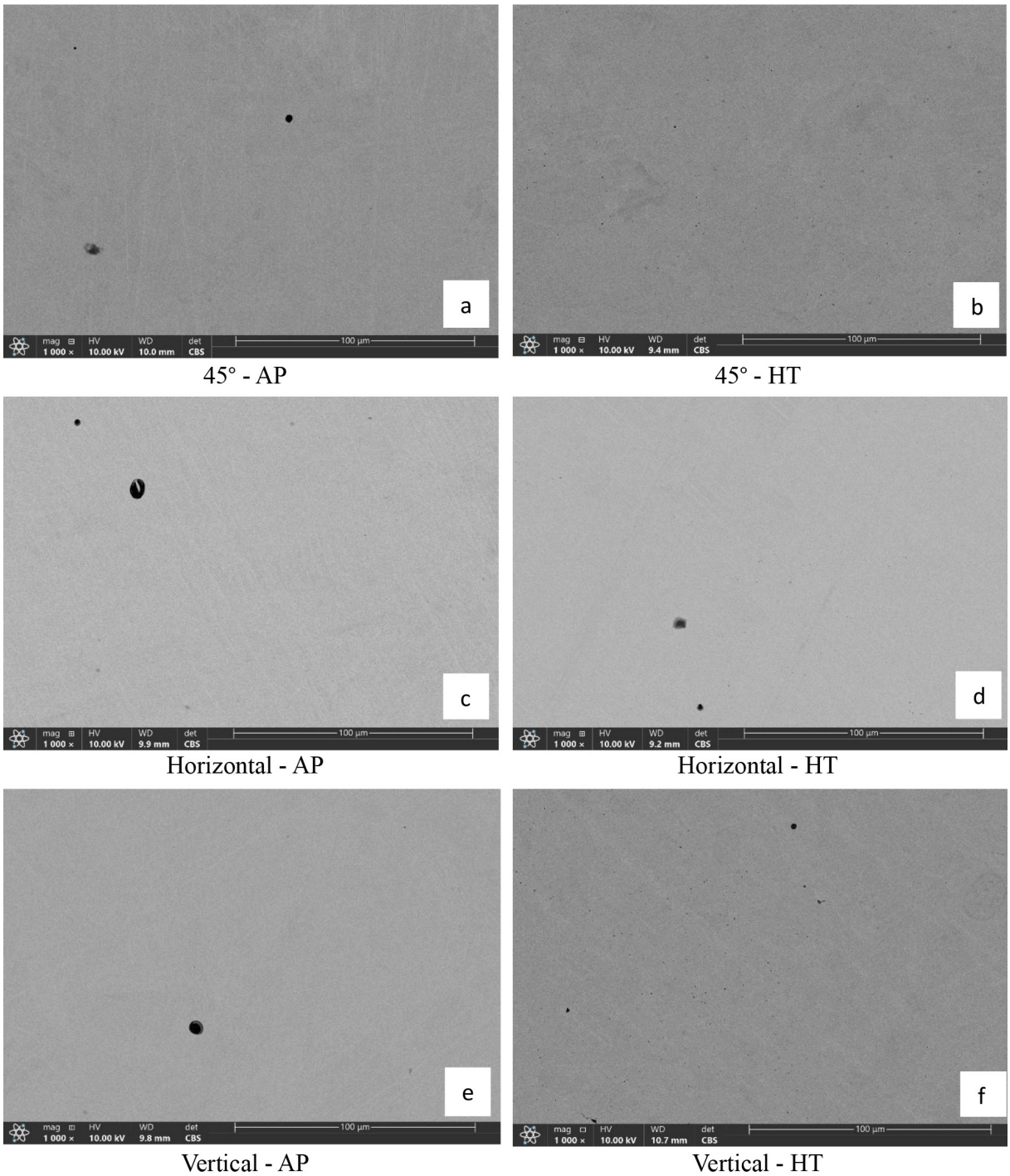


Figure 5. SEM micrographs of 316L stainless steel showing the influence of build orientation (45°, horizontal, vertical) and heat treatment condition (AP and HT); 1,000× magnification

However, SEM observations in Figure 5(d) show that relatively large pores remained visible after heat treatment, and the heat-treated horizontal specimen did not exhibit the same densely dispersed population of fine pores observed in the 45° HT condition.

The total detected pore area decreased slightly from 8.05 µm² to 7.34 µm², while the area fraction changed only marginally from 0.028% to 0.026%. Therefore, for the horizontal orientation, heat treatment did not substantially increase the total projected pore fraction. Instead, the main changes were associated with reduced mean pore size and improved pore shape regularity. Circularity increased from 0.880 to 0.955, and solidity increased from 0.883 to 0.941, indicating that the detected pores became more rounded and compact after heat treatment.

Nevertheless, the persistence of larger isolated pores suggests that the observed difference in the pore population in the horizontal specimens showed a less pronounced shift towards fine, uniformly dispersed features.

The different behaviour of the horizontal specimens may be related to the thermal conditions imposed by the build geometry during LB-PBF. In the horizontal orientation, the layer-wise cross-sectional area exposed to the laser is larger than in inclined or vertically oriented cylindrical geometries. These geometrical differences may influence local heat accumulation, melt-pool stability, and remelting history.

The mechanical response of the horizontal samples also changed after heat treatment. The ultimate tensile strength decreased from 700.5 MPa to 622.0 MPa, while the 0.2% proof strength decreased more strongly, from 618.0 MPa to 346.0 MPa. At the same time, maximum elongation increased from 31.8% to 39.6%, corresponding to an increase of approximately 24% relative to the as-printed condition. The interpretation of this strength–ductility response is discussed together with the other build orientations. The increased elongation may partly reflect improved pore circularity and solidity, although porosity refinement alone does not fully explain the mechanical response.

In the as-printed condition, the horizontal specimens exhibited clearly visible melt-pool features, as shown in Figure 9(c). The morphology reflects the layer-wise nature of the LB-PBF process and the repeated thermal cycling associated with the stripe scanning strategy. Figure 9(d) shows that, after heat treatment, the microstructure exhibited a refined appearance relative to the as-printed state, but the homogenisation was not complete. Larger, elongated, and irregular grain-boundary features remained visible. This indicates that heat treatment modified the printed microstructure but did not fully eliminate the anisotropic features inherited from the build process. The presence of such retained structural features may also contribute to the distinct pore evolution observed in the horizontal condition.

Overall, the horizontal condition showed a more moderate AP–HT difference, characterised by a higher pore count, reduced characteristic pore size and more regular pore morphology, while comparatively larger pore features remained in the HT condition.

Vertical build orientation

SEM observations of the vertical metallographic specimens show a pronounced change in the pore population after heat treatment, as presented in Figure 5(e,f) and quantified in Table 4. In the as-printed condition, the mean number of detected pores was 10.60 pores per analysed field, whereas after heat treatment this value increased markedly to 325.21 pores per field. This indicates a substantial increase in the number of detected pore features after heat treatment.

At the same time, the mean pore area decreased from 0.769 μm² in the as-printed condition to 0.108 μm² after heat treatment. Similar changes were observed in the other size-related descriptors, with decreases in mean perimeter, Feret diameter, and minimum Feret diameter. These results indicate a transition from a small number of larger detected features towards a more highly populated field of finer features.

Unlike the horizontal specimens, the vertical heat-treated condition exhibited a strong increase in total detected pore area and area fraction. The total pore area increased from 7.60 μm² to 36.62 μm², while the area fraction increased from 0.026% to 0.128%. Therefore, although individual pore size decreased, the overall projected pore fraction increased after heat treatment. This suggests that the heat-treated vertical specimens should not be interpreted as having reduced porosity; rather, they exhibited a different pore population characterised by a substantially higher number of smaller, more dispersed pores.

The SEM images support this quantitative trend. In the as-printed vertical specimen, Figure 5(e), only a limited number of pores were visible, but these pores were relatively large. After heat treatment, Figure 5(f), the analysed surface contained numerous fine micropores distributed across the observed field. This behaviour demonstrates a pronounced difference in the apparent post-mortem pore morphology and distribution between the AP and HT vertical conditions.

The pore shape descriptors also changed after heat treatment. Circularity increased from 0.891 to 0.980, while solidity increased from 0.884 to 0.952. These values indicate that the detected pores became more rounded and more compact in projection. The increase in circularity and solidity, together with the decrease in Feret diameter and perimeter, indicates a finer and more regular detected pore morphology in the HT condition.

Nevertheless, the observed increase in pore count should be interpreted as an apparent section-based change in the detected pore population rather than direct evidence of complete 3D pore fragmentation.

The mechanical response of the vertical tensile samples changed substantially after heat treatment. The ultimate tensile strength decreased from 611.0 MPa to 559.5 MPa, while the 0.2% proof strength decreased from 574.5 MPa to 357.5 MPa. Maximum elongation increased from 42.4% to 55.3%, corresponding to an increase of approximately 30% relative to the as-printed condition.

Optical microscopy observations further support the presence of heat-treatment-induced microstructural modification. In the as-printed condition, Figure 9(e), the vertical specimens showed clearly visible melt-pool boundaries and relatively large, irregular grains. After heat treatment, Figure 9(f), the microstructure appeared more refined, with smaller grains and reduced melt-pool contrast. This indicates that heat treatment altered the printed microstructural state, leading to a more homogenised appearance relative to the as-printed condition.

Overall, the vertical condition showed a pronounced AP–HT difference in both the detected post-mortem pore population and microstructural appearance, with the HT condition exhibiting more numerous, smaller and more regular pore features together with reduced melt-pool contrast.

Comparative discussion – influence of build orientation and heat treatment on porosity and mechanical behaviour

The combined results from SEM observations, optical microscopy, ImageJ-based pore analysis, and tensile testing demonstrate that both build orientation and heat treatment strongly affected the defect state and mechanical response of LB-PBF 316L stainless steel. The mean pore descriptors in Table 4 show that the as-printed specimens were generally characterised by a relatively low pore count and larger projected pore dimensions, whereas the heat-treated conditions showed a shift towards smaller and more geometrically regular pores. However, the extent of this transformation was strongly orientation dependent. This behaviour is consistent with the broader understanding that LB-PBF defect formation is governed by local melt-pool stability, thermal gradients, remelting history, and scan-track overlap [15, 30].

It should be emphasised that the SEM/ImageJ analysis represents two-dimensional post-mortem defect populations, which may include both process-induced pores and deformation-assisted voids. Therefore, differences between AP and HT conditions are interpreted comparatively and not as direct evidence of individual-pore fragmentation, growth, or redistribution during heat treatment.

The most pronounced changes after heat treatment were observed for the 45° and vertical specimens. In the 45° orientation, pore count increased from 7.25 to 150.38 pores per analysed field, while the mean pore area decreased from 0.532 to 0.075 μm². Similarly, in the vertical orientation, pore count increased from 10.60 to 325.21 pores per field, while the mean pore area decreased from 0.769 to 0.108 μm². These trends show that the HT conditions were characterised by a greater number of smaller detected features. The decrease in Feret diameter and perimeter, together with the increase in circularity and solidity, further indicates that the pores became more rounded and compact in projection. By contrast, the horizontal orientation showed a more moderate change: pore count increased only from 11.13 to 19.88 pores per field, while the total pore area and area fraction decreased slightly. This indicates a less pronounced difference in pore size and distribution between the AP and HT conditions than that observed for the 45° and vertical orientations.

The field-to-field coefficient of variation of pore area fraction also indicated differences in local heterogeneity among the material conditions. The values decreased from 1.69 to 0.54 for the 45° condition and from 1.53 to 0.76 for the vertical condition after heat treatment, whereas the horizontal condition showed a smaller change from 1.24 to 1.09. These values describe variation among the analysed SEM fields and should not be interpreted as a direct measure of within-field pore clustering.

This orientation-dependent response is also evident in Figure 6, which shows the relative changes induced by heat treatment. The 45° and vertical specimens exhibited large increases in pore count and substantial reductions in mean pore size, whereas the horizontal specimens showed a weaker change in pore population. This suggests that the observed AP–HT differences may reflect not only the heat-treatment condition but also orientation-dependent differences in the defect populations established during

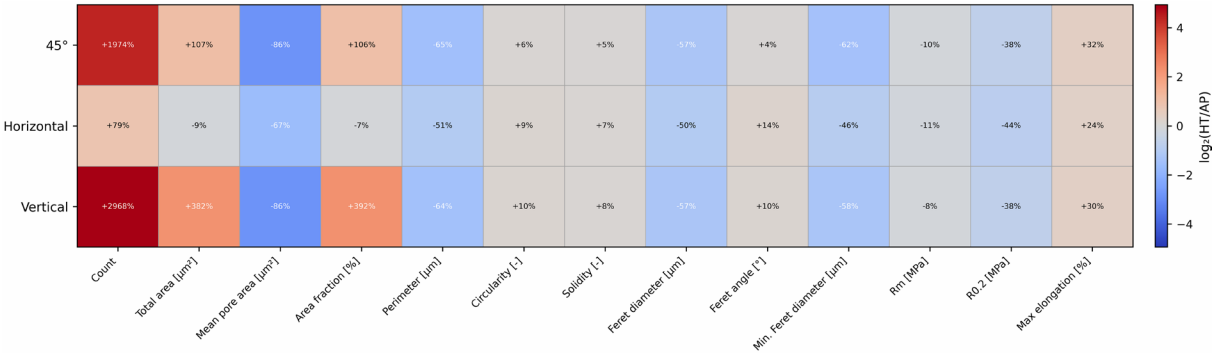


Figure 6. Relative changes from AP to HT for each build orientation. Cell colours represent $\log_2$(HT/AP), while the annotations show percentage change relative to the AP condition

the manufacturing process. Since all specimens were processed using the same nominal LB-PBF parameters—corresponding to a nominal volumetric energy density of approximately 78 J/mm³—the observed differences are more likely associated with orientation-dependent thermal conditions. Although these nominal parameters were identical, the geometry presented in each deposited layer differed with build orientation, affecting the instantaneous layer cross-sectional area, scan-vector length, time between successive local heating events, and thermal conduction path to the substrate. These geometrical differences can modify local heat accumulation, cooling conditions, melt-pool overlap, and remelting history.

The optical microscopy images in Figure 9 further support the role of the printed microstructural state. In the as-printed condition, all orientations exhibited melt-pool-related features, although their appearance varied with build orientation. The fish-scale morphology and melt-pool boundary contrast reflect the repeated melting and solidification cycles intrinsic to LB-PBF. These features should not be interpreted as strengthening mechanisms by themselves; rather, they are macroscopic evidence of the underlying rapid solidification microstructure, including cellular structures, chemical segregation, high dislocation density, and anisotropic thermal gradients. Such hierarchical microstructures are widely reported for additively manufactured 316L and are commonly associated with the elevated strength of the as-printed state [31,32].

After heat treatment, the optical micrographs showed reduced melt-pool contrast and a more homogenised appearance. These observations are consistent with heat-treatment-induced modification of the LB-PBF microstructure, which may involve recovery, residual-stress relief, and partial reduction of the solidification-induced substructure. However, the present OM and SEM observations alone are insufficient to confirm complete recrystallisation or full dissolution of all LB-PBF-induced microstructural features. Therefore, the heat-treated microstructures should be described conservatively as showing reduced melt-pool boundary contrast and apparent microstructural homogenisation. Confirmation of recrystallisation would require EBSD-based grain orientation mapping.

The tensile data in Table 5 indicate that heat treatment reduced strength in all build orientations while increasing elongation. The decrease in 0.2% proof strength was particularly pronounced: from 620.5 to 387.5 MPa for the 45° samples, from 618.0 to 346.0 MPa for the horizontal samples, and from 574.5 to 357.5 MPa for the vertical samples. In contrast, maximum elongation increased from 37.8% to 49.7%, from 31.8% to 39.6%, and from 42.4% to 55.3% for the 45°, horizontal, and vertical samples, respectively. This strength–ductility shift is consistent with modification of the as-printed microstructural state and cannot be explained by the observed porosity differences alone. Recovery, residual-stress relief, and reduced cellular strengthening may contribute to this response. Similar strength reductions and ductility improvements after heat treatment of LB-PBF 316L have been reported in the literature, where yield behaviour was linked primarily to microstructural features, while ductility and failure were more sensitive to pore morphology, orientation, and distribution [25].

The pore morphology results nevertheless provide important context for the ductility response. Large, irregular, elongated, or clustered pores can act as local stress concentrators and promote earlier void nucleation, growth, and coalescence.

Table 5. Tensile properties of as-printed and heat-treated LB-PBF 316L samples. Values are reported as the arithmetic mean ± half-range of two measurements

Sample	R_m [MPa]	$R_{0.2}$ [MPa]	Elongation at fracture [%]
45° AP	683.5 ± 13.5	620.5 ± 18	37.8 ± 1.5
45° HT	618 ± 18.5	387.5 ± 15.5	49.7 ± 2.5
Horizontal AP	700.5 ± 14	618 ± 12.5	31.8 ± 1.3
Horizontal HT	622 ± 24.5	346 ± 16.5	39.6 ± 1.6
Vertical AP	611 ± 12.5	574.5 ± 17	42.4 ± 1.3
Vertical HT	559.5 ± 17	357.5 ± 16	55.3 ± 2.6

In this respect, pore size, shape, and spatial distribution are more mechanically relevant than pore count alone. The present results show that heat treatment generally increased circularity and solidity while reducing Feret diameter and perimeter, indicating a shift towards more regular pore morphologies. This trend may have contributed to the increased elongation observed after heat treatment, particularly in the 45° and vertical specimens. However, this effect should be regarded as complementary to the microstructural softening caused by heat treatment, rather than as the sole reason for the improved ductility. The distinction between gas/keyhole pores and lack-of-fusion defects is also important, since spherical pores and irregular LoF-type defects are known to affect tensile behaviour differently [33,34].

Figure 7 provides a useful overview of the relative behaviour of the six analysed conditions. The normalised heatmap shows that the heat-treated vertical condition had the highest pore count and area fraction, while the horizontal as-printed condition had the highest mean pore area and Feret diameter. This reinforces the conclusion that pore count alone is not an adequate indicator of defect severity. A large number of fine, rounded pores may be less damaging than a smaller number of larger or more irregular defects, depending on their distribution and orientation relative to the loading direction. The horizontal specimens are particularly relevant in this respect, as SEM observations showed that relatively large pores remained visible after heat treatment, despite improvements in circularity and solidity.

The Pearson correlation map in Figure 8 shows correlations between measured parameters within the present dataset. Because the correlation analysis was based on only six condition-level mean values, the resulting coefficients should be interpreted cautiously as exploratory indicators of association rather than as statistically robust relationships. For example, pore count and total pore area showed negative correlations with strength and positive correlations with elongation, whereas mean pore area, Feret diameter, perimeter, and minimum Feret diameter showed the opposite trend. These correlations should not be interpreted as evidence that larger pores improve strength. Instead, they reflect the strong

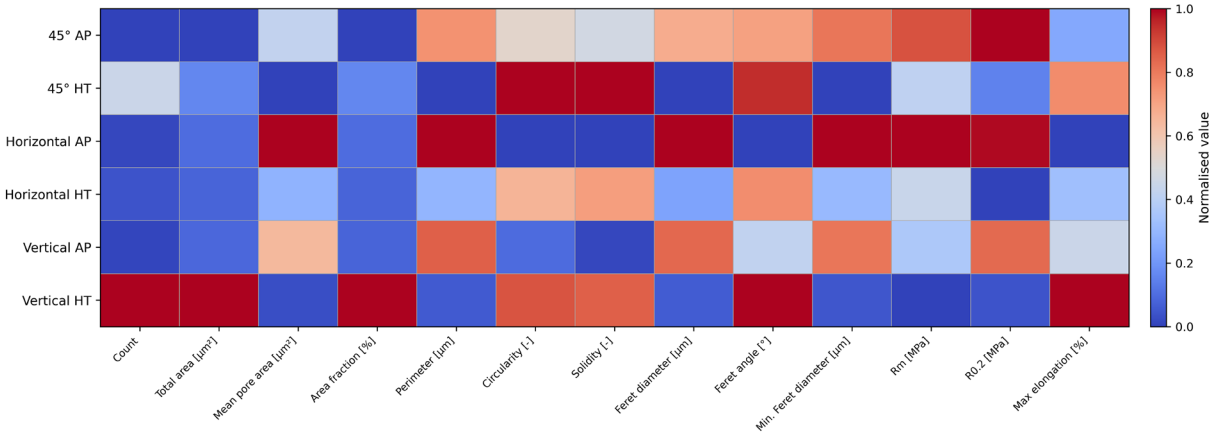


Figure 7. Normalised heatmap of ImageJ-derived pore characteristics and tensile properties

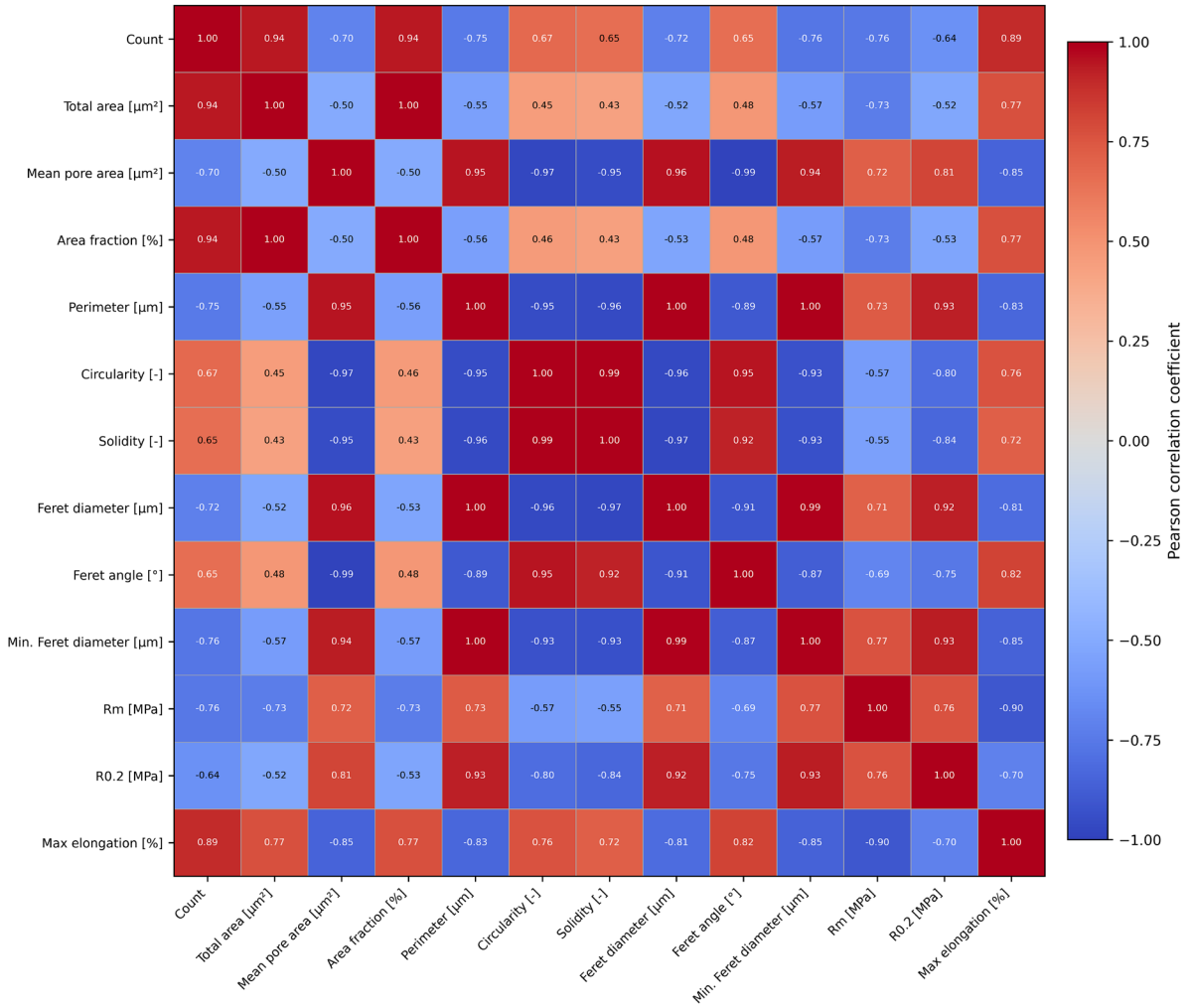


Figure 8. Pearson correlation heatmap of pore descriptors and tensile properties based on six condition-level mean values

confounding effect of heat treatment: the as-printed specimens generally retained higher strength while also containing larger pores, whereas the heat-treated specimens showed reduced strength, higher elongation, and a finer pore population. Thus, Figure 8 supports the interpretation that mechanical behaviour is governed by the coupled influence of microstructural state and defect morphology, rather than by a single pore descriptor.

Overall, the comparative analysis indicates that build orientation was associated with differences in the detected post-mortem pore population and in the AP–HT response. The 45° and vertical orientations showed pronounced AP–HT shifts towards a finer and more dispersed detected pore population, whereas the horizontal orientation showed a more limited shift and retained larger pore features. At the same time, all orientations showed reduced strength and increased elongation after heat treatment, indicating that the observed strength reduction is consistent with modification of the LB-PBF microstructural state, while pore morphology and spatial distribution may have contributed to damage initiation and ductility. Comparable orientation-dependent trends have been reported for DMLS-fabricated 17-4 PH stainless steel, where samples built at 45° exhibited higher maximum tensile strength than vertically built samples, whereas the vertical orientation showed greater deformation to failure. Computed tomography analysis in that study also indicated a slightly lower porosity fraction for the 45° orientation than for the vertical orientation, together with larger individual pores in the vertically built material (Figure 9). Although the alloy system and processing conditions differ from those examined here, the consistency of these trends provides supporting

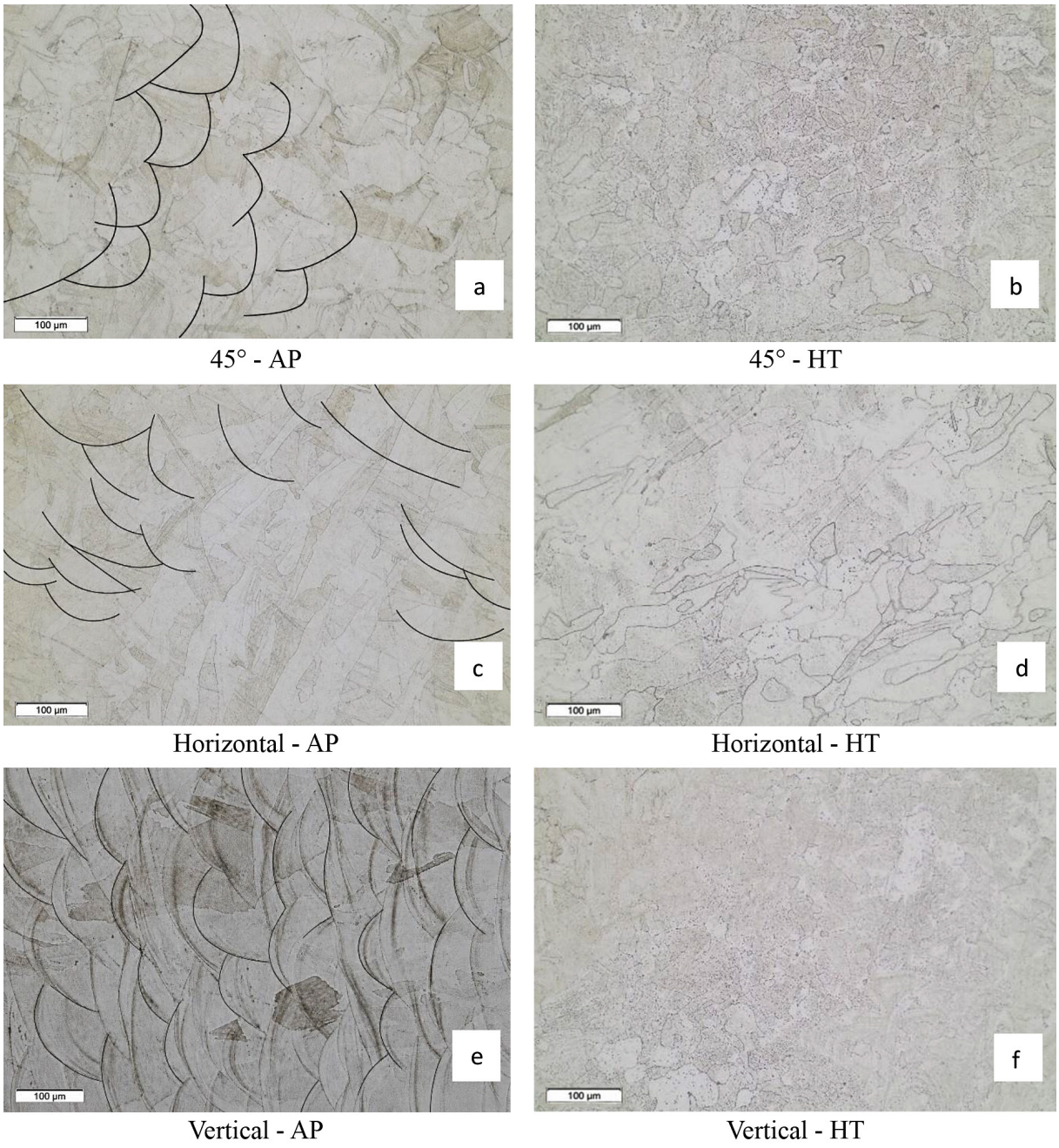


Figure 9. Optical micrographs of 316L stainless steel showing the influence of build orientation (45°, horizontal, vertical) and heat treatment condition (AP and HT). Melt-pool boundaries in the as-printed condition are marked with black lines.

evidence that build orientation affects both defect populations and the associated strength–ductility response across additively manufactured stainless steels [35]. The present results therefore support a coupled interpretation: microstructural features and residual-stress state may contribute substantially to the strength response, whereas pore morphology, size, and distribution presumably play a critical role in ductility and failure behaviour.

CONCLUSIONS

This study showed that build orientation and post-process heat treatment were associated with distinct post-mortem pore characteristics and tensile responses in LB-PBF 316L stainless steel.

The largest AP–HT differences in the detected pore population occurred in the 45° and vertical conditions. Mean pore count increased from 7.25 to 150.38 pores per field for the 45° condition and

from 10.60 to 325.21 pores per field for the vertical condition, while mean pore area decreased from 0.532 to 0.075 μm² and from 0.769 to 0.108 μm², respectively. The horizontal condition exhibited a considerably smaller increase in pore count, from 11.13 to 19.88 pores per field, and retained comparatively larger pore features.

The ultimate tensile strength, R_m, decreased from 683.5 to 618.0 MPa, from 700.5 to 622.0 MPa, and from 611.0 to 559.5 MPa for the 45°, horizontal, and vertical orientations, respectively. In parallel, elongation increased from 37.8 to 49.7%, from 31.8 to 39.6%, and from 42.4 to 55.3%. These trends are consistent with heat-treatment-induced modification of the LB-PBF microstructural state, while the present experiments do not independently quantify recovery or residual-stress relief.

Pore count alone was insufficient to describe the observed defect state. The combined use of projected pore area, circularity, solidity and Feret dimensions provided additional information on the morphology of the post-mortem defect population and revealed clear orientation-dependent differences between AP and HT conditions.

Because the porosity analysis was performed on two-dimensional metallographic specimens prepared after tensile testing, the detected features may include both process-induced pores and deformation-assisted voids. The observed AP–HT differences therefore represent comparative post-mortem defect states and should not be interpreted as direct three-dimensional evidence of individual-pore refinement, fragmentation or redistribution during heat treatment.

REFERENCES

1. DebRoy T., Wei H.L., Zuback J.S., Mukherjee T., Elmer J.W., Milewski J.O., Beese A.M., Wilson-Heid A., De A., Zhang W. Additive manufacturing of metallic components – Process, structure and properties. Progress in Materials Science 2018; 92: 112–224. https://doi.org/10.1016/j.pmatsci.2017.10.001
2. Herzog D., Seyda V., Wycisk E., Emmelmann C. Additive manufacturing of metals. Acta Materialia 2016; 117: 371–392. https://doi.org/10.1016/j.actamat.2016.07.019
3. Jaggannagari S.R., Kan W.H., Chiu L.N.S., Proust G., Huang A., Gan Y., Annabattula R.K. Numerical and experimental analysis of powder bed homogeneity through multi-layer spreading in additive manufacturing. Additive Manufacturing 2025; 97: 104571. https://doi.org/10.1016/j.addma.2024.104571
4. Sabzi H.E., Rivera-Diaz-del-Castillo P.E.J. Composition and process parameter dependence of yield strength in laser powder bed fusion alloys. Materials & Design 2020; 195: 109024. https://doi.org/10.1016/j.matdes.2020.109024
5. Hooper P.A. Melt pool temperature and cooling rates in laser powder bed fusion. Additive Manufacturing 2018; 22: 548–559. https://doi.org/10.1016/j.addma.2018.05.032
6. Rafi H.K., Pal D., Patil N., Starr T.L., Stucker B.E. Microstructure and Mechanical Behavior of 17-4 Precipitation Hardenable Steel Processed by Selective Laser Melting. Journal of Materials Engineering and Performance 2014; 23: 4421–4428. https://doi.org/10.1007/s11665-014-1226-y
7. Gan Z., Lian Y., Lin S.E., Jones K.K., Liu W.K., Wagner G.J. Benchmark Study of Thermal Behavior, Surface Topography, and Dendritic Microstructure in Selective Laser Melting of Inconel 625. Integrating Materials and Manufacturing Innovation 2019; 8: 178–193. https://doi.org/10.1007/s40192-019-00130-x
8. Wang R., Shi H., Gu J., He X., Zhang P., Yu Z., Yan H., Lu Q. Additive manufacturing of metal lattice structures: A comprehensive review of technologies, mechanical properties, applications, and future trends. Materials Today Physics 2025; 59: 101933. https://doi.org/10.1016/j.mtphys.2025.101933
9. Snow Z., Nassar A.R., Reutzel E.W. Invited Review Article: Review of the formation and impact of flaws in powder bed fusion additive manufacturing. Additive Manufacturing 2020; 36: 101457. https://doi.org/10.1016/j.addma.2020.101457
10. Du C., Zhao Y., Jiang J., Wang Q., Wang H., Li N., Sun J. Pore defects in Laser Powder Bed Fusion: Formation mechanism, control method, and perspectives. Journal of Alloys and Compounds 2023; 944: 169215. https://doi.org/10.1016/j.jallcom.2023.169215
11. Hojjatzadeh S.M.H., Parab N.D., Guo Q., Qu M., Xiong L., Zhao C., Escano L.I., Fezzaa K., Everhart W., Sun T., Chen L. Direct observation of pore formation mechanisms during LPBF additive manufacturing process and high energy density laser welding. International Journal of Machine Tools and Manufacture 2020; 153: 103555. https://doi.org/10.1016/j.ijmactools.2020.103555
12. Leung C.L.A., Luczyniec D., Guo E., Marussi S., Atwood R.C., Meisnar M., Saunders B., Lee P.D. Quantification of Interdependent Dynamics during Laser Additive Manufacturing Using X-Ray Imaging Informed Multi-Physics and Multiphase Simulation. Advanced Science 2022; 9(36): 2203546. https://doi.org/10.1002/advs.202203546
13. Sai M.M.K., Mandal A. Prediction of laser process

parameters for diverse melting regimes in laser powder bed fusion process through normalized enthalpy framework. Optics & Laser Technology 2025; 192: 114111. https://doi.org/10.1016/j.optlastec.2025.114111

14. Plessis du A. Effects of process parameters on porosity in laser powder bed fusion revealed by X-ray tomography. Additive Manufacturing 2019; 30: 100871. https://doi.org/10.1016/j.addma.2019.100871
15. Shrestha S., Chou K. Formation of keyhole and lack of fusion pores during the laser powder bed fusion process. Manufacturing Letters 2022; 32: 19–23. https://doi.org/10.1016/j.mfglet.2022.01.005
16. Wu Z., Basu D., Meyer J.L.L., Larson E., Kuo R., Beuth J., Rollett A. Study of Powder Gas Entrapment and Its Effects on Porosity in 17-4 PH Stainless Steel Parts Fabricated in Laser Powder Bed Fusion. JOM 2021; 73: 177–188. https://doi.org/10.1007/s11837-020-04491-z
17. Dwivedi M., Arunachalam N. Effect of build orientation on mechanical and physical properties of Ti-6Al-4V LPBF additively manufactured thin structures without support. Manufacturing Letters 2025; 44: 936–941. https://doi.org/10.1016/j.mfglet.2025.06.110
18. Williams R.J., Vecchiato F., Kelleher J., Wenman M.R., Hooper P.A., Davies C.M. Effects of heat treatment on residual stresses in the laser powder bed fusion of 316L stainless steel: Finite element predictions and neutron diffraction measurements. Journal of Manufacturing Processes 2020; 57: 641–653. https://doi.org/10.1016/j.jmapro.2020.07.023
19. Hastie J.C., Kartal M.E., Carter L.N., Attallah M.M., Mulvihill D.M. Classifying shape of internal pores within AlSi10Mg alloy manufactured by laser powder bed fusion using 3D X-ray micro computed tomography: Influence of processing parameters and heat treatment. Materials Characterization 2020; 163: 110225. https://doi.org/10.1016/j.matchar.2020.110225
20. Nayak S.K., Jinoop A.N., Paul C.P., Kumar V.A., Subburaj D., Singh R., Bindra K.S. On the hot isostatic pressing of Inconel 625 structures built using laser powder bed fusion at higher layer thickness. The International Journal of Advanced Manufacturing Technology 2022; 120: 4065–4078. https://doi.org/10.1007/s00170-022-08960-4
21. Kaletsch A., Qin S., Herzog S., Broeckmann C. Influence of high initial porosity introduced by laser powder bed fusion on the fatigue strength of Inconel 718 after post-processing with hot isostatic pressing. Additive Manufacturing 2021; 47: 102331. https://doi.org/10.1016/j.addma.2021.102331
22. Cegan T., Pagac M., Jurica J., Skotnicova K., Hajnys J., Horsak L., Soucek K., Krpec P. Effect of Hot Isostatic Pressing on Porosity and Mechanical Properties of 316 L Stainless Steel Prepared by the Selective Laser Melting Method. Materials 2020; 13: 4377. https://doi.org/10.3390/ma13194377
23. Pu Q., Qian J., Zhang Y., Yang S., Huang H., Chao Q., Fan G. The Influence of Post-Treatment on Micropore Evolution and Mechanical Performance in AlSi10Mg Alloy Manufactured by Laser Powder Bed Fusion. Materials 2024; 17: 4319. https://doi.org/10.3390/ma17174319
24. Shin W.-S., Son B., Song W., Sohn H., Jang H., Kim Y.-J., Park C. Heat treatment effect on the microstructure, mechanical properties, and wear behaviors of stainless steel 316L prepared via selective laser melting. Materials Science and Engineering: A 2021; 806: 140805. https://doi.org/10.1016/j.msea.2021.140805
25. Ronneberg T., Davies C.M., Hooper P.A. Revealing relationships between porosity, microstructure and mechanical properties of laser powder bed fusion 316L stainless steel through heat treatment. Materials & Design 2020; 189: 108481. https://doi.org/10.1016/j.matdes.2020.108481
26. He L., Qin J., Lou B., Zhu Z., Ni J., Hu X., Cao W. Ultra-rapid (3 min) solution treatment for quasi-isotropic SLM 316 L: Regulation of microstructure and defect evolution. Materials Characterization 2026; 233: 116136. https://doi.org/10.1016/j.matchar.2026.116136
27. Petrousek P., Kocisko R., Kasperkevicova A., Csik D., Dzunda R. Effect of Thermomechanical Processing on Porosity Evolution and Mechanical Properties of L-PBF AISI 316L Stainless Steel. Metals 2025; 15: 789. https://doi.org/10.3390/met15070789
28. Feng Z., Pan H., Wu W., Wang Z., Jiang P. Impact of Heat Treatment and Building Direction on Selective Laser-Melted 316L Stainless Steel: Microstructure and Mechanical Properties. Materials 2025; 18: 32. https://doi.org/10.3390/ma18010032
29. Lim Y., Jeon C., Lee Y.-S., Jo I. Influence of Build Orientation and Heat Treatment on the Microstructure and Mechanical Properties of SUS316L Fabricated by Selective Laser Melting. Metals 2025; 15: 971. https://doi.org/10.3390/met15090971
30. Narasimharaju S.R., Zeng W., See T.L., Zhu Z., Scott P., Jiang X., Lou S. A comprehensive review on laser powder bed fusion of steels: Processing, microstructure, defects and control methods, mechanical properties, current challenges and future trends. Journal of Manufacturing Processes 2022; 75: 375–414. https://doi.org/10.1016/j.jmapro.2021.12.033
31. Wang Y.M., Voisin T., McKeown J.T., Ye J., Calta N.P., Li Z., Zeng Z., Zhang Y., Chen W., Roehling T.T., Ott R.T., Santala M.K., Depond P.J., Matthews M.J., Hamza A.V., Zhu T. Additively manufactured

hierarchical stainless steels with high strength and ductility. Nature Materials 2018; 17: 63–71. https://doi.org/10.1038/nmat5021

32. Bertsch K.M., Meric de Bellefon G., Kuehl B., Thoma D.J. Origin of dislocation structures in an additively manufactured austenitic stainless steel 316L. Acta Materialia 2020; 199: 19–33. https://doi.org/10.1016/j.actamat.2020.07.063
33. Kan W.H., Chiu L.N.S., Lim C.V.S., Zhu Y., Tian Y., Jiang D., Huang A. A critical review on the effects of process-induced porosity on the mechanical properties of alloys fabricated by laser powder bed fusion. Journal of Materials Science 2022; 57: 9818–9865. https://doi.org/10.1007/s10853-022-06990-7
34. Vallejo N.D., Kljestan N., Ayers N., Knezevic M., Sohn Y. Flaw type dependent tensile properties of 316L stainless steel additively manufactured by laser powder bed fusion. Results in Materials 2022; 15: 100315. https://doi.org/10.1016/j.rinma.2022.100315
35. Deroszewska M., Saraczyn R., Cisowski A., Kowaluk T., Borowski T., Petru J., Myszka D. Investigation of the impact of porosity of elements made using DMLS 3D printing technology and various printing angles on the mechanical properties and microstructure of 17-4 PH stainless steel. Journal of Achievements in Materials and Manufacturing Engineering 2023; 121: 187–203. https://doi.org/10.5604/01.3001.0054.3050